Chinese Chemical Letters 31 (2020) 2747–2751

Contents lists available at ScienceDirect

Chinese Chemical Letters

journal homepage: www.elsevier.com/locate/cclet

Communication

Honeycomb-like g-C_3N_4/CeO_{2-x} nanosheets obtained *via* one step hydrothermal-roasting for efficient and stable Cr(VI) photo-reduction

Yanan Liu[a], Zhangfeng Shen[a], Jialing Song[a,b], Huilan Qi[b], Chaochuang Yin[b], Xuhui Zou[b], Qineng Xia[a], Lifeng Cui[b], Xi Li[a], Yangang Wang[a,*]

[a] College of Biological Chemical Science and Engineering, Jiaxing University, Jiaxing 314001, China
[b] Department of Environmental Science and Engineering, University of Shanghai for Science and Technology, Shanghai 200093, China

ARTICLE INFO

Article history:
Received 6 April 2020
Received in revised form 15 May 2020
Accepted 9 June 2020
Available online 17 June 2020

Keywords:
One step hydrothermal-roasting method
g-C_3N_4/CeO_{2-x}
Oxygen vacancies
Cr(VI) reduction
Visible light photocatalysis

ABSTRACT

Graphitic carbon nitride (g-C_3N_4)-based materials are regarded as one of the most potential photocatalysts for utilizing solar energy. In this work, we reported a facile one step *in-situ* hydrothermal-roasting method for preparing honeycomb-like g-C_3N_4/CeO_2 nanosheets with abundant oxygen vacancies (g-C_3N_4/CeO_{2-x}). The hydrothermal-roasting and incomplete-sealed state can (i) generate an *in-situ* reducing atmosphere (CO, N_2, NH_3) to tune the concentration of oxygen vacancies in CeO_2; (ii) beneficial to prevent continuous growth of g-C_3N_4 and results in honeycomb-like g-C_3N_4/CeO_{2-x} hybrid nanosheets. What is more, the g-C_3N_4/CeO_{2-x} photocatalyst exhibited extended photoresponse range, increased specific surface area and obviously enhanced separation efficiency of photogenerated electron-hole pairs. As a proof-of-concept application, the optimized g-C_3N_4/CeO_{2-x} nanosheets could achieve 98% removal efficiency for Cr(VI) under visible light irradiation ($\lambda \geq 420$ nm) within 2.5 h, which is significantly better than those of pure g-C_3N_4 and CeO_2. This work provides a new idea for more rationally designing and constructing g-C_3N_4-based catalysts for efficient extended photochemical application.

Hexavalent chromium (Cr(VI)), highly toxic and easily gets into the food chains and hence in the biological body, is considered as one of most severe contaminants of surface and ground water [1]. The enrichment of Cr(VI) *in vivo* can lead to a series of severe health problems, such as hereditary genetic defect and canceration [2]. Thus, eliminating Cr(VI) from water or reducing Cr(VI) concentration to acceptable level is of critical significance to biodiversity and human health. Cr(VI) can be precipitated and removed from water by the methods of adsorption, chemical precipitation, ion exchange and reduction from Cr(VI) to Cr(III) [3]. Among them, photocatalytic reduction of Cr(VI) to Cr(III) has been considered an ideal and feasible strategy for water governance due to its environmental friendliness and relatively effectiveness [4]. What is more, the less harmful trivalent chromium is regarded as an essential nutrient component for human, plant and animal metabolism [3]. Various materials have been developed for photocatalytic removal of Cr(VI) from water, such as TiO_2, ZnO, CdS [5–8]. However, these conventional photocatalytic materials still show many disadvantages, like the complicated preparation and low quantum efficiency.

Recently, graphitic carbon nitride (g-C_3N_4), a metal-free polymeric semiconductor, has attracted tremendous attention owing to its good features of cheapness, thermal and chemical stability, tunable electronic structure, as well as the unique 2D feature coupled with narrowed band gap [9–11]. Unfortunately, the photocatalytic activity of g-C_3N_4 is still hindered by two primary characteristics, namely, comparatively unsatisfactory utilization of solar light and too-rapid recombination rate of photogenerated carriers [12]. To settle these problems, construction of a semiconductor-semiconductor heterojunction through coupling with other semiconductor has been proven to be an effective approach. The obtained heterojunctions can not only enhance the light-absorption capacity of g-C_3N_4, but also improve the separation efficiency of photoinduced electron-hole pairs, resulting in prolonged charge carrier lifetime and enhanced photocatalytic activity.

Cerium dioxide (CeO_2), as one of the reactive rare earth oxides, has shown promising photocatalytic activity for the degradation of various organic dye pollutants [13,14]. This is because CeO_2 is capable to interact with electron-rich surface heteroatoms *via* weak coordination, which creates new electron donor, strengthens

* Corresponding author.
E-mail address: ygwang8136@mail.zjxu.edu.cn (Y. Wang).

https://doi.org/10.1016/j.cclet.2020.06.016

UV light absorbance and favors photocatalytic reactions [15]. Tian *et al.* successfully designed CeO_2/g-C_3N_4 hybrid materials by *in-situ* co-pyrolysis the mixture of $Ce(IO_3)_3$ and melamine [16]. Liang *et al.* synthesized hollow heterostructured g-C_3N_4@CeO_2 photocatalysts for enhanced photocatalytic CO_2 reduction [17]. Nevertheless, the reported g-C_3N_4/CeO_2 heterostructures have ignored the importance of rich oxygen vacancies, large BET surface area and intimate interface interaction in photocatalytic reaction.

In the present study, we designed a simple and cost-effective one step roasting method for preparing honeycomb structure g-C_3N_4/CeO_{2-x} nanosheets (Fig. S1 in Supporting information). Unlike traditional calcination methods that the raw materials were just put into a crucible and then calcined in muffle furnace, the aqueous solution of raw materials was poured into crucibles, and each crucible was sealed with three sheets of tin-foil in our method. At the beginning of the synthesis, the raw materials were subjected to hydrothermal treatment through the interaction of aqueous solution, which is beneficial to the urea and $Ce(NO_3)_3{\cdot}6H_2O$ fully mix at the molecular level. Subsequently, the mixtures have undergone a calcination process at 550 °C for 4 h. In the hydrothermal-roasting process, the incomplete-sealed state could not only generate *in-situ* reducing atmosphere (CO, N_2, NH_3) to promote the production of oxygen vacancies in g-C_3N_4/CeO_{2-x}, but also be beneficial to the strong interactions formed between CeO_{2-x} and g-C_3N_4, which prevents the continuous growth of g-C_3N_4 and results in honeycomb-like g-C_3N_4/CeO_{2-x} nanosheet structure.

The crystal structures of as-prepared g-C_3N_4, CeO_2 and g-C_3N_4/CeO_{2-x} were measured by X-ray diffraction (XRD) (Fig. 1A). For pure g-C_3N_4, there are two obvious diffraction peaks at 13.0° and 27.4°, which agree with the results reported in the literature [18]. The characteristic diffraction peak of g-C_3N_4 gradually weaken and even disappear with increasing the content of $Ce(NO_3)_3{\cdot}6H_2O$ during the preparation process. This phenomenon indicates that the graphite-like planar stacked structure of the interlayer stacking of g-C_3N_4 was not maintained in the g-C_3N_4/CeO_{2-x}, especially at a high introduced amount of $Ce(NO_3)_3{\cdot}6H_2O$ [19]. In addition, the real content of CeO_2 in the g-C_3N_4/CeO_{2-x} composites performed by thermal gravimetrical (TG) analysis was similar to the theoretical value (6 wt%) (Fig. S2 in Supporting information), and no obvious diffraction peaks of CeO_2 can be observed in all g-C_3N_4/CeO_{2-x} samples, indicating the small particles and well dispersion of CeO_2 in the g-C_3N_4 matrix [20].

The nanosheet structure of g-C_3N_4/CeO_{2-x} was also proved through scanning electron microscopy (SEM) and transmission electron microscopy (TEM). The SEM image in Fig. 1B reveals that the representative g-C_3N_4/CeO_{2-x}-2 is composed of disorderly stacked layers. What's more, these nanosheets have honeycomb-like structure as shown in the TEM images (Figs. 1C–E). During the hydrothermal-roasting process, the thermal motion of abundant released steam (*e.g.* CO, N_2, H_2O and NH_3) in the incomplete sealed system enriched the pore structure of g-C_3N_4, leading to high surface area (pure g-C_3N_4: 70.68 m^2/g, g-C_3N_4/CeO_{2-x}-2: 129.21 m^2/g) (Fig. S3 in Supporting information) [21]. The interface structure of g-C_3N_4/CeO_{2-x} was observed by high-resolution TEM (HRTEM). As descripted in Fig. 1F, the lattice spacing of 0.32 nm, corresponding to (111) plane of CeO_2, is observed. The small CeO_2 nanoparticles with size of about 5 nm are well distributed on the nanosheet and intimately integrated on the surface of g-C_3N_4. This kind of structure can offer good interfacial properties between CeO_2 and g-C_3N_4 substrate for synergistic electron transfer utilized in photocatalytic applications. Thus, the porous honeycomb-like nanosheets structure not only provides large number of active sites for the photocatalytic reaction, but also shortens the charge carrier diffusion distance by increasing the interfacial transport kinetics.

To gain insight into the surface compositions and chemical states of pure g-C_3N_4, CeO_2 and g-C_3N_4/CeO_{2-x}-2 nanosheets, X-ray photoelectron spectroscopy (XPS) was carried out [22]. The XPS survey spectrum of g-C_3N_4/CeO_{2-x}-2 nanosheets in Fig. S4 (Supporting information) verifies the existence of C, N, O and Ce. As seen from Fig. 2A, the peak at 288.6 eV (C-$(N)_3$) in g-C_3N_4/CeO_{2-x}-2 nanosheet were found slightly higher than that of pure g-C_3N_4 (288.2 eV) [23]. A reverse binding energy change can be also observed from the XPS spectra of N 1s (Fig. 2B). Compared with N 1s binding energies at 398.5 eV, 400.1 eV and 400.9 eV for g-C_3N_4, the N 1s peaks for g-C_3N_4/CeO_2-2 shift to 398.2 eV, 399.4 eV and 400.6 eV, respectively [18]. The binding energy shift of C 1s and N 1s indicate the formation of strong electronic interactions between CeO_{2-x} with g-C_3N_4 [24].

High-resolution Ce 3d spectrum in Fig. 2C can be fitted into eight components. The sub-bands labeled u′ and v′ are assigned to Ce^{3+} species and the u, u″, u‴, v, v″ and v‴ peaks refer to Ce^{4+} cation [25]. The ratio of Ce^{3+} to Ce^{4+} in pure CeO_2 is estimated to be about 19.84%, indicating the formation of oxygen vacancy in CeO_2 lattice because of the semi-closed and oxygen-poor environment. In

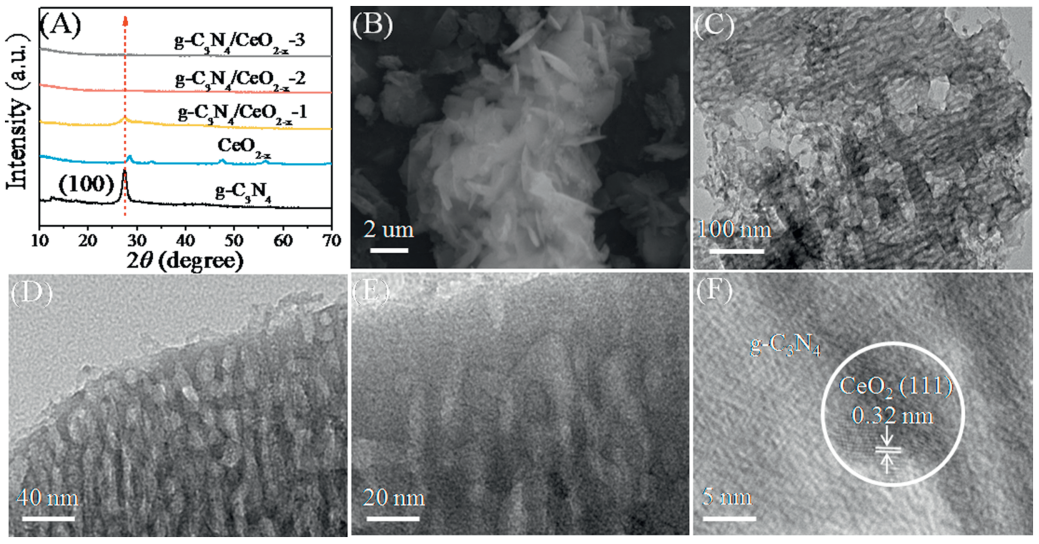

Fig. 1. XRD patterns (A) of the as-synthesized g-C_3N_4, CeO_2 and g-C_3N_4/CeO_{2-x}. SEM (B), TEM (C-E) and HRTEM (F) images of the representative g-C_3N_4/CeO_{2-x}-2.

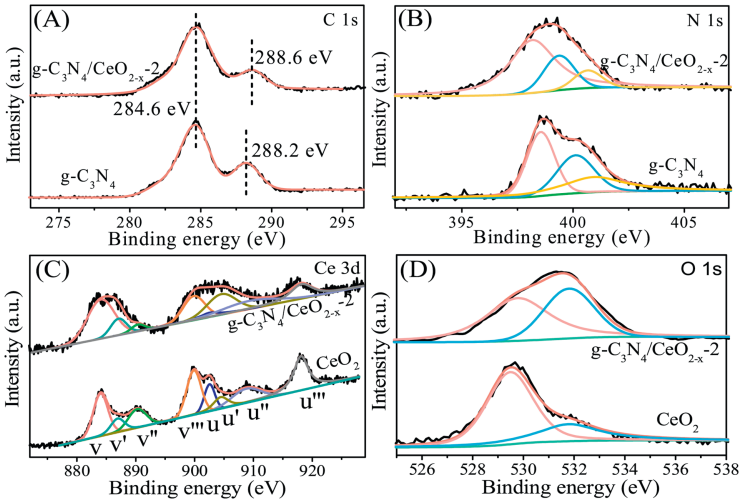

Fig. 2. High-resolution XPS spectra of C 1s (A), N 1s (B), Ce 3d (C) and O 1s (D) for pure g-C_3N_4, CeO_2 and g-C_3N_4/CeO_{2-x}-2.

comparison with pure CeO_2, the ratio of Ce^{3+}/Ce^{4+} in g-C_3N_4/CeO_{2-x}-2 increases to 24.23%. In addition, the content of oxygen deficient and hydroxyl groups (−OH) on the surface of CeO_{2-x} (the high binding energy component in O 1s peak (Fig. 2D)) was increased after compounding with g-C_3N_4. The increase of oxygen vacancies in g-C_3N_4/CeO_{2-x} can be attributed to the NH_3, produced during the decomposition process of urea, partly reducing the *in-situ* generated CeO_{2-x} [26]. The presence of strong electronic interactions and increased oxygen vacancies again demonstrates the well establishment of g-C_3N_4/CeO_{2-x} heterojunction. Moreover, the FT-IR spectra (Fig. S5 in Supporting information) can further confirm the g-C_3N_4/CeO_{2-x} heterojunction formation.

The nature of the oxidation state (Ce^{3+}/Ce^{4+}) in CeO_2 and g-C_3N_4/CeO_{2-x}-2 was further investigated by spin trapping electron paramagnetic resonance technique (EPR). As shown in Fig. 3A, pure CeO_2 shows a weak symmetrical EPR signal for Ce^{3+} at g = 2.00. The trigonal site of the Ce^{3+} ion can be easily realized near an oxygen vacancy [27]. In comparison with CeO_2, g-C_3N_4/CeO_{2-x}-2 gives a similar but more intense symmetrical EPR signal, belonging to oxygen vacancies as the present of urea in the one-step hydrothermal-roasting process increased the ratio of Ce^{3+}/Ce^{4+}. The effect of oxygen vacancies and morphology on optical absorption properties and of as-prepared samples were studied *via* a UV–vis diffuse reflectance spectrometer (DRS). It can be clearly seen that the pure g-C_3N_4 has an absorption edge at 465 nm, while the CeO_2 sample displays a similar absorption edge but lower light absorption intensity in the entire spectral region (Fig. 3B). In comparison with CeO_2 and g-C_3N_4, the absorption edge of g-C_3N_4/CeO_{2-x}-2 exhibits an obviously red shift and much narrower band gap of 1.58 eV (Fig. S6A in Supporting information) due to the further enriched oxygen vacancies in g-C_3N_4/CeO_{2-x}-2 hybird composite and the strong interfacial interaction between CeO_2 and g-C_3N_4. Furthermore, combine Mott-Schottky analysis (Fig. S6B in Supporting information) and the physicochemical properties (Table S1 in Supporting information) of as-prepared samples, we can know that the CeO_2 and g-C_3N_4 have well matching band

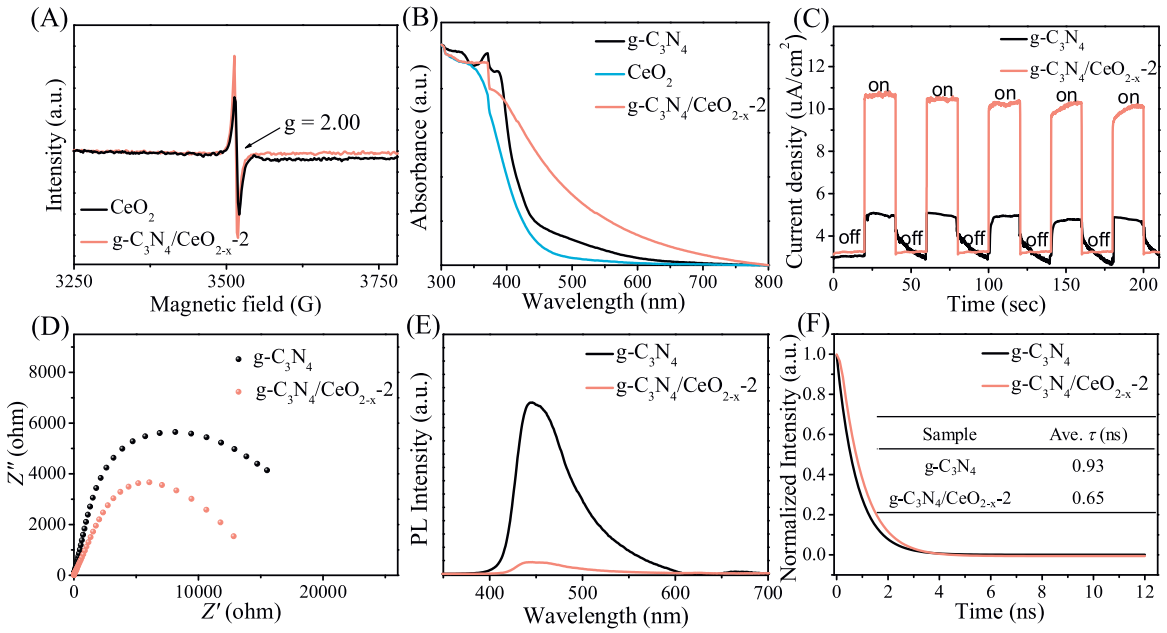

Fig. 3. (A) The X-band EPR spectra of the CeO_2 and g-C_3N_4/CeO_{2-x}-2 samples recorded at room temperature. (B) The UV–vis DRS spectra of g-C_3N_4, CeO_2 and g-C_3N_4/CeO_{2-x}-2; (C) The photocurrent response, (D) Nyquist impedance plots, (E) PL spectra (excitation at 315 nm) and (F) TRPL spectra (excitation at 315 nm, emission at 430 nm) measured at room temperature of g-C_3N_4 and g-C_3N_4/CeO_{2-x}-2.

potentials. The enlarged spectral response range and matched band potentials of g-C_3N_4/CeO_{2-x}-2 heterostructure would be beneficial to the generation, separation and transfer of electron-hole pairs.

The efficient transfer, migration and separation of photogeneration charge carriers of photocatalyst were studied by transient photocurrent response curves (Fig. 3C) and electrochemical impedance spectroscopy (EIS) measurements (Fig. 3D). It is clearly that the g-C_3N_4/CeO_{2-x}-2 shows substantially enhanced photocurrent intensity compared to the pure g-C_3N_4. The higher photocurrent density and smaller semicircle radius in g-C_3N_4/CeO_{2-x}-2, indicating the constructed honeycomb-like g-C_3N_4/CeO_{2-x}-2 nanosheets can enhance the light absorption and the photogeneration charge carriers separation and transfer [28,29]. The electron transfer and recombination behavior of photocatalysts are further studied *via* steady-state photoluminescence (PL) emission spectra and time-resolved PL spectroscopy (TRPL). In generally, a higher PL intensity indicates a higher recombination rate of photogenerated electron-hole pairs, a shorter decay lifetime indicates faster interfacial charge transfer through non-radiative quenching pathways [30,31]. As presented in Fig. 3E, there is an obviously decrease in the PL intensity of g-C_3N_4/CeO_{2-x}-2 compared to that of pure g-C_3N_4. The corresponding average emission lifetime for g-C_3N_4 and g-C_3N_4/CeO_{2-x}-2 are calculated to be 0.93 and 0.65 ns, respectively (Fig. 3F). Overall, the existed intimate interface between g-C_3N_4 and CeO_{2-x} could efficiently retard the recombination of charge carriers and would enhance the photocatalytic activity.

The photocatalytic activities of the honeycomb-like g-C_3N_4/CeO_{2-x} nanosheets were explored through monitoring the photocatalytic reduction of Cr(VI) in aqueous solution under visible light irradiation ($\lambda \geq 420$ nm) (Fig. 4A). The reduction of Cr(VI) hardly occurs in the absence of photocatalyst, and pure g-C_3N_4 demonstrates a relatively poor catalytic performance due to the rapid recombination (RB) of photocatalytic electron-hole pairs. After introduction of CeO_2 into g-C_3N_4, remarkable reduction performance of Cr(VI) was observed. Among all g-C_3N_4/CeO_{2-x} samples, g-C_3N_4/CeO_{2-x}-2 exhibits the highest photocatalytic reduction efficiency of Cr(VI), where 98% of Cr(VI) can be reduced within 2.5 h. In addition, the g-C_3N_4/CeO_{2-x}-2 nanosheets also displays excellent stability for the photoreduction of Cr(VI). As shown in Fig. 4B, only a slight decline is observed after four cycles. The decreased efficiency can be contributed to the inevitable catalyst loss during reusing. The FT-IR results of g-C_3N_4/CeO_{2-x}-2 before and after photocatalytic experiment are shown in Fig. S7 (Supporting information). There is no clear change after the photocatalytic reaction, which further confirmed the stability of g-C_3N_4/CeO_{2-x}.

To further understand the photocatalysis mechanism of reduction of Cr(VI), we carried out the control experiments with adding isopropanol (IPA, $(CH_3)_2CHOH$, a scavenger for $^{\bullet}OH$ radicals) and 1,4-benzoquinone (BQ, $C_6H_4O_2$, a scavenger for $O_2^{\bullet-}$ radicals) (Fig. S8 in Supporting information) [7]. It is obvious that the adding IPA into the reaction system almost completely inhibit the photocatalytic reduction of Cr(VI), suggesting that the $^{\bullet}OH$ is the main active radical for transfer and consumption of holes. While the reduction was significantly enhanced in presence of BQ, which is attributed to competitive reactions between Cr(VI) reduction and $O_2^{\bullet-}$ radicals formation; at the same time, the H_2O_2 could be produced by $O_2^{\bullet-}$ radical and H^+, generated in CB of CeO_{2-x}, could also oxidize the Cr(III) back to Cr(VI) *in-situ* during the reaction process [32,33].

On the basis of above-mentioned analysis and results, the schematic illustrations of the free carriers' generation, separation, migration and reaction under visible-light irradiation are proposed and given in Figs. 4C and D. The pure CeO_2 can not generate electron-hole pairs under visible light irradiation because of the wide band gap (3.28 eV) [34]. The band gap of CeO_2 is reduced significantly to 2.48 eV after introducing oxygen vacancies (Table S1). Furthermore, the strong interactions formed between CeO_{2-x} and g-C_3N_4 during hydrothermal-roasting process will be beneficial to the transfer and separation of photoinduced electron-hole pairs. When g-C_3N_4/CeO_{2-x} nanosheets is irradiated by visible-light, both g-C_3N_4 and CeO_{2-x} can be excited to generate electron-hole pairs. The

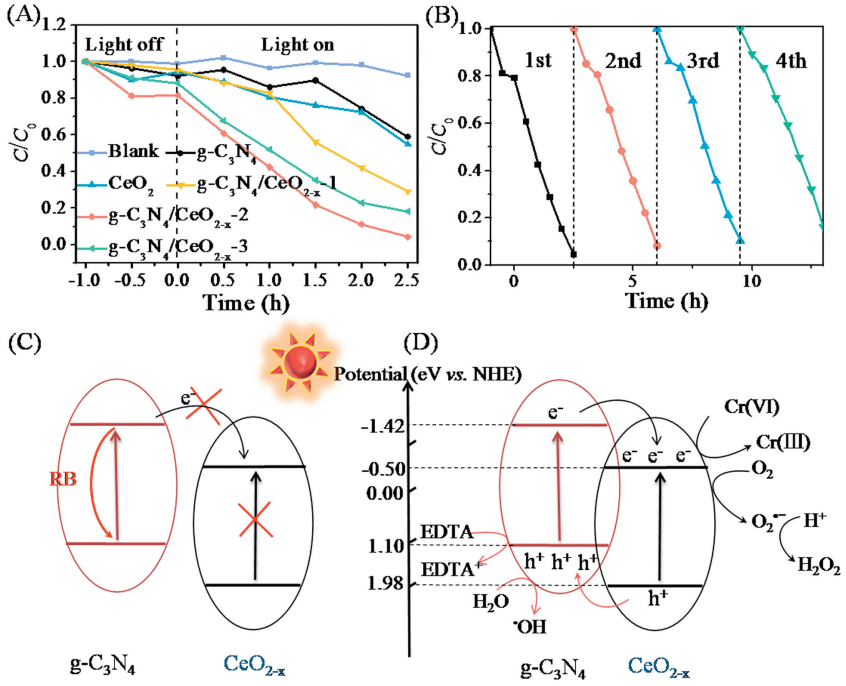

Fig. 4. (A) Photocatalytic reduction curves of the Cr(VI) (pH 3) under visible light irradiation. (B) The reusability of g-C_3N_4/CeO_{2-x}-2 nanosheets for the reduction of Cr(VI). The schematic illustration of the reduction of Cr(VI) on g-C_3N_4/CeO_2 (C) and g-C_3N_4/CeO_{2-x} (D) under visible light irradiation (RB: recombination).

photogenerated electrons in the CB of g-C_3N_4 will migrate to the CB of CeO_{2-x} and directly reduce Cr(VI) to eco-friendly trivalent chromium Cr(III). While the holes will transfer from the VB of CeO_{2-x} to that of g-C_3N_4 and captured by sacrificial agent (EDTA) and −OH, undergoing the oxidation process. Thus, the recombination of electron-hole pairs is suppressed and the photocatalytic Cr(VI) reduction performance is significantly enhanced.

In summary, we have developed a novel one step hydrothermal-roasting method to synthesize honeycomb-like oxygen vacancies-rich g-C_3N_4/CeO_{2-x} nanosheets. Results reveal that the composites have abundant oxygen vacancies, stronger intimate interfacial contact between g-C_3N_4 and CeO_2, large surface area, broadened visible light absorption range, and thus resulting in remarkable photocatalytic activity. Lastly, a possible catalytic mechanism is proposed and discussed in detail. This research not only provides an attractive catalyst for the Cr(VI) photoreduction reaction, but also paves a new facile path to fabricating more highly active photocatalysts for water treatment.

Declaration of competing interest

The authors declare that they have no known competing financial interests or personal relationships that could have appeared to influence the work reported in this paper.

Acknowledgments

This work was carried out with financial supports from the National Natural Science Foundation of China (Nos. 21103024, 61171008), Natural Science Foundation of Zhejiang Province (No. LY19B060006), National Key Research and Development Program of China (No. 2018YFB1502900), and Technology Development Project of Jiaxing University (No. 70518047).

Appendix A. Supplementary data

Supplementary material related to this article can be found, in the online version, at doi:https://doi.org/10.1016/j.cclet.2020.06.016.

References

[1] N.R. Bishnoi, M. Bajaj, N. Sharma, A. Gupta, Bioresour. Technol. Rep. 91 (2004) 305–307.
[2] S.S. Ahluwalia, D. Goyal, Bioresource Technol. 98 (2007) 2243–2257.
[3] M. Owlad, M.K. Aroua, W.A.W. Daud, S. Baroutian, Water Air Soil Pollut. 200 (2009) 59–77.
[4] L.X. Yang, Y. Xiao, S.H. Liu, Y. Li, Q.Y. Cai, et al., Appl. Catal. B 94 (2010) 142–149.
[5] Z.J. Luo, L.L. Qu, J.Z. Jia, Chin. Chem. Lett. 29 (2018) 547–550.
[6] J.K. Yang, S.M. Lee, Chemosphere 63 (2006) 1677–1684.
[7] Y.H. Zhang, Z. Chen, S.Q. Liu, Y.J. Xu, Appl. Catal. B 140-141 (2013) 598–607.
[8] X.J. Liu, L. Pan, T. Lv, G. Zhu, Z. Sun, et al., Chem. Commun. 47 (2011) 11984–11986.
[9] Y.P. Chen, H.Y. Zhang, R. Lu, A.C. Yu, Chin. Chem. Lett. 29 (2018) 543–546.
[10] J.Q. Wen, J. Xie, X.B. Chen, X. Li, Appl. Surf. Sci. 391 (2017) 72–123.
[11] W.J. Ong, L.L. Tan, Y.H. Ng, S.T. Yong, S.P. Chai, Chem. Rev. 116 (2016) 7159–7329.
[12] L. Xu, W.Q. Huang, L.L. Wang, et al., Chem. Mater. 27 (2015) 1612–1621.
[13] M. Aslam, M.T. Qamar, M.T. Soomro, et al., Appl. Catal. B 180 (2016) 391–402.
[14] H.R. Pouretedal, A. Kadkhodaie, Chin. J. Catal. 31 (2010) 1328–1334.
[15] X.J. Lang, X.D. Chen, J.C. Zhao, Chem. Soc. Rev. 43 (2014) 473–486.
[16] N. Tian, H.W. Huang, C.Y. Liu, et al., J. Mater. Chem. A 3 (2015) 17120–17129.
[17] M.F. Liang, T. Borjigin, Y.H. Zhang, et al., Appl. Catal. B: Environ. 243 (2019) 566–575.
[18] S.W. Cao, J.X. Low, J.G. Yu, M. Jaroniec, Adv. Mater. 27 (2015) 2150–2176.
[19] F.X. Cheng, H.N. Wang, X.P. Dong, Chem. Commun. 51 (2015) 7176–7179.
[20] R. Phienluphon, L. Shi, J. Sun, et al., Catal. Sci. Technol. 4 (2014) 3099–3107.
[21] P.J. Yang, H.H. Ou, Y.X. Fang, X.C. Wang, Angew. Chem. Int. Ed. 56 (14) (2017) 3992–3996.
[22] C. Ling, C.L. Yue, R.R. Yuan, et al., Chem. Eng. J. 384 (2020) 123278.
[23] Y.M. He, Y. Wang, L.H. Zhang, B.T. Teng, M.H. Fan, Appl. Catal. B 168-169 (2015) 1–8.
[24] Y.N. Liu, X. Zhou, X. Wang, et al., RSC Adv. 7 (2017) 30080–30085.
[25] Z.M. Liu, J.Z. Zhu, J.H. Li, L.L. Ma, ACS Appl. Mater. Interfaces 6 (2014) 14500–14508.
[26] J.A. Rodriguez, J. Graciani, J. Evans, et al., Angew. Chem. Int. Ed. 48 (2009) 8047–8050.
[27] M.E. Khan, M.M. Khan, Sci. Rep. 7 (2017) 5928.
[28] H.L. Guo, H. Du, Y.F. Jiang, et al., J. Phys. Chem. C 121 (2017) 107–114.
[29] Z.H. Zhang, P. Wang, Energy Environ. Sci. 5 (2012) 6506–6512.
[30] Y.G. Wang, Q.N. Xia, X. Bai, et al., Appl. Catal. B 239 (2018) 196–203.
[31] S. Zhang, L. Wang, C. Liu, et al., Water Res. 121 (2017) 11–19.
[32] A.D. Bokare, W. Choi, Environ. Sci. Technol. 45 (2011) 9332–9338.
[33] J.C. Wang, J. Ren, H.C. Yao, et al., J. Hazard. Mater. 311 (2016) 11–19.
[34] R. Saravanan, S. Joicy, V.K. Gupta, V. Narayanan, A. Stephen, Mater. Sci. Eng. C 33 (2013) 4725–4731.